

Magnetic tuning of the tunnel coupling in an optically active quantum dot molecule

Frederik Bopp,^{1,*} Charlotte Cullip,^{1,*} Christopher Thalacker,¹ Michelle Lienhart,¹ Johannes Schall,² Nikolai Bart,³ Friedrich Sbresny,⁴ Katarina Boos,⁴ Sven Rodt,² Dirk Reuter,⁵ Arne Ludwig,³ Andreas D. Wieck,³ Stephan Reitzenstein,² Filippo Troiani,⁶ Guido Goldoni,^{6,7} Elisa Molinari,^{6,7} Kai Müller,⁴ and Jonathan J. Finley^{1,†}

¹Walter Schottky Institut, School of Natural Sciences, and MCQST,

Technische Universität München, Am Coulombwall 4, 85748 Garching, Germany

²Institut für Festkörperphysik, Technische Universität Berlin, Hardenbergstrae 36, 10623 Berlin, Germany

³Lehrstuhl für Angewandte Festkörperphysik, Ruhr-Universität Bochum, Universitätsstrae 150, 44801 Bochum, Germany

⁴Walter Schottky Institut, School of Computation, Information and Technology, and MCQST,

Technische Universität München, Am Coulombwall 4, 85748 Garching, Germany

⁵Paderborn University, Department of Physics, Warburger Strae 100, 33098 Paderborn, Germany

⁶Centro S3, CNR-Istituto Nanoscienze, Via Campi 213/a, 41125 Modena, Italy

⁷Dipartimento di Scienze Fisiche, Informatiche e Matematiche,

Università di Modena e Reggio Emilia, Via Campi 213/a, 41125 Modena, Italy

(Dated: March 23, 2023)

Self-assembled optically active quantum dot molecules (QDMs) allow the creation of protected qubits via singlet-triplet spin states. The qubit energy splitting of these states is defined by the tunnel coupling strength and is, therefore, determined by the potential landscape and thus fixed during growth. Applying an in-plane magnetic field increases the confinement of the hybridized wave functions within the quantum dots, leading to a decrease of the tunnel coupling strength. We achieve a tuning of the coupling strength by $(53.4 \pm 1.7)\%$. The ability to fine-tune this coupling is essential for quantum network and computing applications that require quantum systems with near identical performance.

Although any physical qubit is susceptible to dephasing, the use of protected qubits offers a way to passively shield the quantum information from its noise environment [1, 2]. Few-spin solid-state qubits are particularly promising in this regard, since they are immune to the dominant electric and magnetic field noise sources to first order [3–5]. Recently, the extension of the spin coherence time by creating a few-spin (e.g., singlet-triplet) qubit has been demonstrated in a vertically stacked pair of optically active quantum dots [6]. Such quantum dot molecules (QDMs) combine the advantages of single quantum dots (QDs), such as robust optical selection rules [7] and dominant emission into the zero-phonon line [8], with the ability to create protected few-spin qubits [5]. They are formed from two vertically stacked QDs separated by a tunneling barrier. At a separation of a few nanometers, the orbital states in the two dots become tunnel coupled with a strength that depends on the separation of the dots and the height of the tunnel barrier [9]. Tunnel coupling facilitates the creation of hybridized symmetric and anti-symmetric few-spin states, which serve as protected qubit eigenstates [10]. The energy splitting between these two states is defined by the tunnel coupling. This makes the coupling strength the main tuning parameter of the solid-state qubit, since it determines the operating rate of quantum gates [11]. However, the thickness and height of the tunnel barrier are fixed during the growth process. By establishing a method for post-growth continuous and reversible

tuning of the tunnel coupling, synchronization of multiple qubits could be enabled to facilitate applications such as quantum networks [12]. In addition, the generation of two-dimensional photonic cluster states for measurement-based quantum computing could be optimized [13, 14].

One approach to control the tunnel coupling post-growth is to apply strain to the system. However, so far only weak energy shifts up to $50 \mu\text{eV}$ have been achieved experimentally [15] while lacking long-term stability [16]. A second approach to tune the tunnel coupling, promising a wider tuning range with higher temporal stability, is to apply a static magnetic field to the QDM. This results in a modification of the orbital part of the carrier wave function and, therefore, control of the tunnel coupling. Over the past decades, several theoretical works have explored the magnetic tuning of symmetric and anti-symmetric orbitals in artificial molecules [17–22]. However, experimental demonstrations have not yet been provided [23, 24] and structure-property relationships are yet to be established. In-plane magnetic fields are predicted to result in a confinement of the orbital part of the wave function along a direction perpendicular to the field direction (diamagnetic response), corresponding to a reduction of the tunnel coupling [19]. To qualitatively illustrate the magnetic field dependence of the wave function, Figure 1 (a) shows a sketch of the electron wave function in a double-well potential without (solid) and with (dashed) magnetic field B applied along the x-direction. The pink (green) wave function $\Psi(z)$ illustrates the lowest symmetric (second lowest, anti-symmetric) eigenstate of a single electron confined in the QDM potential. The solid black lines represent an approximate potential landscape

* These authors contributed equally to this work

† finley@wsi.tum.de

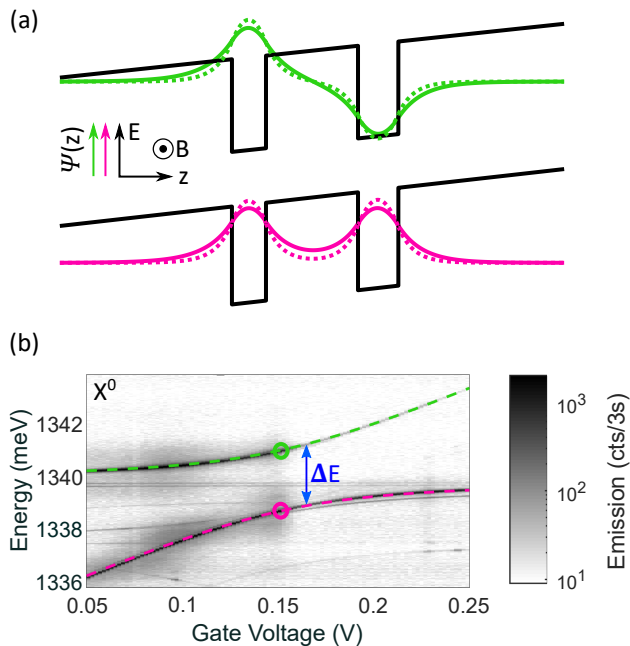


FIG. 1. Tunnel coupling of the neutral exciton (X^0). (a) Schematic of bonding (pink) and anti-bonding (green) wave function $\Psi(z)$ of the lowest and second lowest electron energy eigenstate, respectively, with (dashed) and without (solid) applied in-plane magnetic field B . The solid black lines depict the electron trapping potential along the growth direction z . (b) Voltage-dependent photoluminescence measurement of the X^0 . The energy splitting between the bonding (pink) and anti-bonding (green) eigenstates ΔE is depicted by a blue arrow, while the energy of the tunnel-coupled states is visualized by colored circles.

of the QDM along the growth direction z . The probability density of the charge position inside the two potential wells is predicted to increase at higher magnetic field due to magnetic compression of the wave function [19]. Consequently, the wave function is expelled from the barrier region between the two potentials wells, which effectively reduces the strength of the tunnel coupling.

In this work, we experimentally demonstrate the tunability of the tunnel coupling of an artificial molecule by varying an in-plane magnetic field. We perform magneto-photoluminescence measurements on a single QDM to study the energy splitting between the bonding (BO) and anti-bonding (AB) neutral exciton (X^0) states and hence the tunnel coupling strength. We observe a reduced splitting with increasing magnetic field, which we numerically simulate by modeling a three-dimensional confinement potential and calculating the corresponding single-particle energies and Coulomb interaction between the localized carriers. By applying an electric field along the growth direction, we tune the electronic levels of the two dots into and out of resonance. This allows us to conclusively show that the magnetic field leads to a reduction of the tunnel coupling strength, providing a post-growth control of this parameter.

The QDM investigated in this work consists of two vertically stacked and tunnel-coupled InAs QDs embedded in a GaAs matrix [25]. The neutral exciton (X^0) is used to demonstrate the general reduction of the energy gap between BO and AB eigenstates. Excitation of the neutral exciton is achieved via a continuous wave laser resonant to a higher orbital shell at 1353.6 meV, while the s-shell emission is monitored. To efficiently excite the X^0 state, a two-phase optical and electrical sequence is used for all measurements presented in this letter [26]. The applied gate voltage allows tuning of the energy levels of the two QDs relative to each other. In combination with the tunnel coupling, this allows the hybridization of charge wave functions forming BO and AB eigenstates. An avoided crossing is the result. Figure 1 (b) shows the voltage-dependent photoluminescence of the X^0 state. The eigenenergies corresponding to the BO and AB eigenstates are highlighted by a dashed pink and green fit, respectively. The exciton energies are fitted using a coupled two-state model, including a linear bias and a quadratic contribution proportional to the bias, which accounts for the DC Stark-effect for indirect and direct excitons, respectively [27]. The full description can be found in the Supplemental Material [28].

The voltage at which hybridization of the two wave functions occurs is depicted by colored circles in Figure 1 (b). The minimum energy difference ΔE between the two exciton eigenstates is solely determined by the strength of the tunnel coupling t . Since we work in a regime where the electron can hybridize while the hole remains confined in the upper QD [9], the energy splitting between the BO and AB eigenstates ΔE corresponds to the energy difference between the observed neutral exciton eigenstates. This allows us to analyze the magnetic field-dependent energy separation between the BO and AB wave functions and thus obtain the tunnel coupling between the QDs.

To analyze the in-situ tunability of the tunnel coupling, we apply an in-plane magnetic field along the x-direction (Voigt geometry). Figure 2 (a) shows a magneto-photoluminescence measurement of the BO and AB state at the lowest splitting of 0.15 V. In addition to a diamagnetic shift [29], the magnetic field leads to a mixing of bright and dark exciton states [30] and a Zeeman splitting of the spin states [31]. This results in the occurrence of the four allowed optical transitions for both the BO and AB eigenstates, as shown by the single photoluminescence trace in Figure 2 (a) recorded at 15 T. With an increasing magnetic field, the energy separation ΔE between the eigenstates with the same spin configuration reduces. We define ΔE as the difference between the highest energy transition of the BO and of the corresponding AB eigenstate.

Figure 2 (b) shows the energy splitting ΔE as a function of magnetic field. The blue data points describe the energy separation at 0.15 V obtained from Figure 2 (a). The energy separation between the two eigenstates decreases with increasing magnetic field. In order to un-

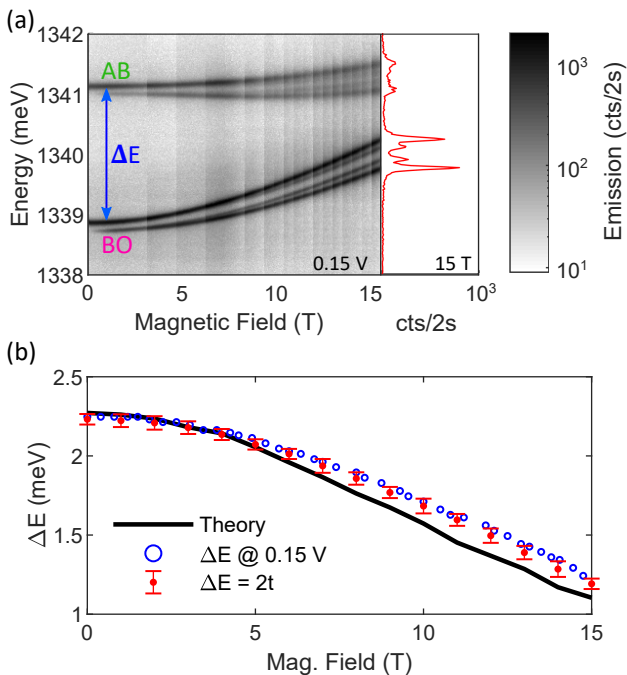


FIG. 2. (a) Magneto-photoluminescence measurement in the tunnel-coupling regime at 0.15 V. The energy splitting ΔE between the bonding (BO) and anti-bonding (AB) eigenstate is illustrated by a blue arrow. The red solid line shows the emission spectrum at 15 T. (b) ΔE , the energy splitting, as function of the magnetic field. The blue data points indicate the energy splitting between the highest energy transitions of the BO and the AB eigenstate at 0.15 V. The red data points are extracted from fitting the voltage-dependent energy splitting. The black solid line shows the numerically predicted energy splitting ΔE .

ambiguously identify the observed transitions, we complement the experimental results with numerical calculations, performed within the envelope-function and the effective-mass approach [32]. The single particle energies and eigenstates are obtained by diagonalizing on a real-space grid of 524 288 points a Hamiltonian that includes a kinetic and a potential contribution:

$$H_{\chi}(\mathbf{r}) = \frac{1}{2m_{\chi}^*} \left(-i\hbar\nabla + \frac{q_{\chi}}{c} \mathbf{A} \right)^2 + V_{\chi}(\mathbf{r}), \quad (1)$$

where $\mathbf{A} = \frac{1}{2}\mathbf{B} \times \mathbf{r}$ is the vector potential, $\chi = e, h$ specifies the particle type and its charge ($q_h = -q_e = |e|$), and m_{χ}^* is the effective mass. The confinement potential includes a parabolic in-plane contribution, $V_{xy,\chi}(x, y) = \frac{1}{2}m_{\chi}^*\omega_{\chi}^2(x^2 + y^2)$, and a double square well in the vertical (z) direction. In particular, the two wells have widths of $d_1 = 2.7$ nm and $d_2 = 2.9$ nm, matching the height of the bottom and top QD, respectively. We note that the dot heights were precisely fixed at these values using the In-flush method [33]. Similarly, the barrier between the two dots was defined during growth and fixed at $l = 7.3$ nm. The height of the barrier is set to $V_0 = 690$ meV, corresponding to the conduction band offset of strained

InAs and GaAs [34]. In addition, the potential includes a linear term $V_{bias,\chi} = q_{\chi}\mathcal{E}z$, with $\mathcal{E} = 3.63$ meV/nm to account for the electric field.

We include the Coulomb interaction perturbatively, and identify the energy of the lowest (first excited) exciton state with the sum of the electron ground state energy, the hole ground state energy, and the direct Coulomb matrix element involving these single-particle states. Further details are provided in the Supplemental Material [28].

The black solid curve in Figure 2 (b) shows the numerically obtained energy splitting ΔE as a function of the strength of the in-plane magnetic field. We obtain an excellent qualitative agreement between experimental and theoretical results. Quantitative differences may result from simplifications in the applied three-dimensional potential.

The magnetic field leads to an enhanced confinement of the charges in the potential wells along the growth direction z , which is associated with a reduction of the electron wave function density inside the tunneling barrier. Thus, the coupling strength decreases with increasing magnetic field. In the presented magnetic field range we observe a decrease of the splitting of the avoided crossing by $(53.4 \pm 1.7)\%$, which corresponds to an absolute energy shift of (-1.04 ± 0.05) meV and a change of the tunnel coupling strength from $t = (1.12 \pm 0.02)$ meV to (0.60 ± 0.02) meV. This is a factor of $21\times$ higher than what could be previously achieved by strain tuning the device [15].

As the magnetic field is increased, the decrease in ΔE and hence the tunnel coupling should be maximal in the center of the avoided crossing. Thus, we continue to analyze ΔE close to and away from the avoided crossing to show conclusively that the reduction of ΔE is indeed caused by a reduction of the tunnel coupling. Therefore, we measured ΔE for different DC gate voltages tracking over the avoided crossing.

Figure 3 (a) shows ΔE as a function of the gate voltage around the avoided crossing at 0 T (black points) and 15 T (blue points). The solid lines result from fitting the data with the difference of the eigenenergies calculated from the coupled two-state model. Both fits show a minimum at the center voltage of the avoided crossing, depicted by the vertical dashed lines. V_C marks the center voltage of the avoided crossing at 0 T. As before, ΔE is reduced at 15 T compared to 0 T. This results in a reduced tunneling coupling strength, represented by the fit parameter t . At V_C the energy splitting is $\Delta E = 2t$, which allows the extraction of the minimum splitting from the applied fit. The red data points in Figure 2 (b) show the minimum energy splitting for different magnetic fields. While the fitted and measured ΔE are in excellent agreement at low magnetic fields, a small deviation is observed for higher fields. This is caused by a magnetic field-dependent shift of V_C . The inset in Figure 3 (a) shows the evolution of V_C with increasing magnetic field. The observed voltage shift of the tunnel

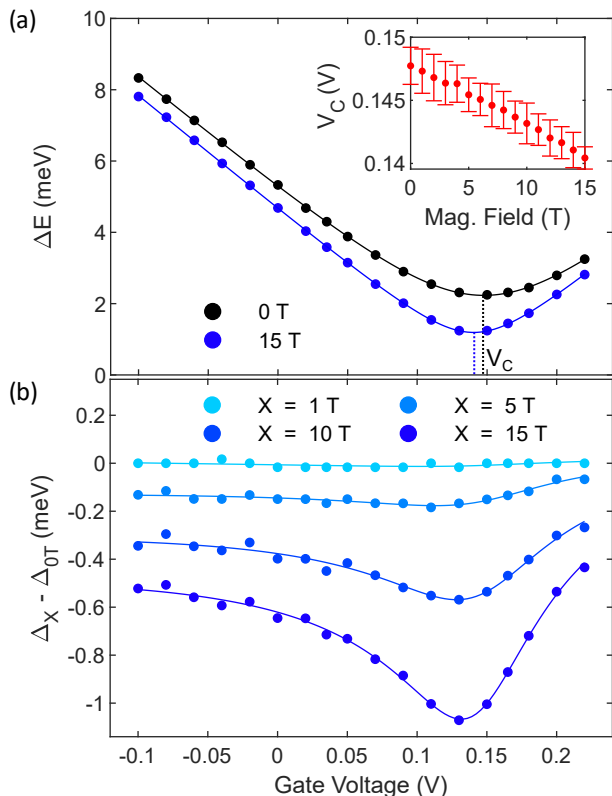


FIG. 3. (a) ΔE as a function of the gate voltage at 0 T (black dots) and 15 T (blue dots). Solid lines visualize the fit of the energy splitting. V_C describes the voltage, where ΔE is minimal. The inset shows V_C as function of the magnetic field. (b) Difference of ΔE with and without applied magnetic field as a function of the gate voltage. The solid lines show the difference between the fits applied in (a).

coupling originates from the different sizes of the two individual QDs. By increasing the magnetic field and thus the confinement of the charge, the eigenenergies of the two QDs encounter different energy shifts. As a result, a lower gate voltage is required to attain the coupling condition. Thus, V_C decreases with increasing magnetic field.

To demonstrate the reduction in energy splitting at the avoided crossing, we analyze the difference of ΔE with and without an applied magnetic field. Figure 3 (b) shows the voltage-dependent difference $\Delta_{XT} - \Delta_{0T}$, with $X \in \{1, 5, 10, 15\}$. The fitted curves (solid lines) are obtained by subtracting the difference of the fitted eigenenergies in Figure 3 (a). The asymmetry of the curve is caused by the change of V_C with increasing magnetic field, as discussed before. The data presented

exhibits a minimum of the energy difference at the avoided crossing. This minimum confirms that the variation of the energy splitting is indeed maximal at the avoided crossing. Thus, we can conclude that the applied magnetic field reduces the tunnel coupling between the two quantum dots.

In summary, we have demonstrated a reduction in the energy splitting between BO and AB eigenstates of a QDM by applying in-plane magnetic fields. This corresponds to a reduction in the tunnel coupling strength between the two QDs. Fitting the energy difference between the eigenstates of the system to the voltage and magnetic field-dependent measurements allows quantification of the variation of the tunnel coupling strength. We obtain a wide tuning range of $(53.4 \pm 1.7)\%$ with a maximum tuning rate of $(-101 \pm 6) \mu\text{eV}/\text{T}$. The decrease of the absolute energy splitting is $(1.04 \pm 0.05) \text{meV}$. Our results confirm several theoretical predictions [17–22] and demonstrate that in-plane magnetic fields enable the tuning of the tunnel coupling in QDMs.

The tunability of the tunnel coupling is crucial for controlling the eigenstates of solid-state qubits in QDMs. The presented results allow optimization of the gate operations for the generation of two-dimensional photonic cluster states [13]. Moreover, tuning the eigenenergies of a qubit facilitates its synchronization with other qubits and thus their entanglement to enable multi-qubit networks. These results are generally applicable to other artificial molecules, e.g. in two-dimensional materials with a similar trapping potential [17].

ACKNOWLEDGMENTS

The authors gratefully acknowledge financial support from the German Federal Ministry of Education and Research (BMBF) via Q.Link.X (16KIS0874, 16KIS086), QR.X (16KISQ027, 16KISQ014, 16KISQ012 and 16KISQ009), MOQUA (13N14846), the Horizon 2020 research and innovation program of the European Union under grant agreement 862035 (QLUSTER) and the Deutsche Forschungsgemeinschaft (DFG, German Research Foundation) via SQAM (FI947-5-1), DIP (FI947-6-1), and the Excellence Cluster MC-QST (EXC-2111, 390814868). F.B. gratefully acknowledges the Exploring Quantum Matter (ExQM) programme funded by the State of Bavaria. FT and EM acknowledge financial support from the European Commission through the project IQubits (Call: H2020FETOPEN20182019202001, ProjectID: 829005).

[1] D. A. Lidar, I. L. Chuang, and K. B. Whaley, Decoherence-free subspaces for quantum computation, *Physical Review Letters* **81**, 2594 (1998).

[2] B. Douot and L. B. Ioffe, Physical implementation of protected qubits, *Reports on Progress in Physics* **75**, 072001 (2012).

- [3] J. R. Petta, A. C. Johnson, J. M. Taylor, E. A. Laird, A. Yacoby, M. D. Lukin, C. M. Marcus, M. P. Hanson, and A. C. Gossard, Coherent manipulation of coupled electron spins in semiconductor quantum dots, *Science* **309**, 2180 (2005).
- [4] M. Stopa and C. M. Marcus, Magnetic field control of exchange and noise immunity in double quantum dots, *Nano Letters* **8**, 1778 (2008).
- [5] K. M. Weiss, J. M. Elzerman, Y. L. Delley, J. Miguel-Sanchez, and A. Imamoglu, Coherent two-electron spin qubits in an optically active pair of coupled InGaAs quantum dots, *Phys. Rev. Lett.* **109**, 107401 (2012).
- [6] K. X. Tran, A. S. Bracker, M. K. Yakes, J. Q. Grim, and S. G. Carter, Enhanced spin coherence of a self-assembled quantum dot molecule at the optimal electrical bias, *Phys. Rev. Lett.* **129**, 027403 (2022).
- [7] Y. Benny, S. Khatsevich, Y. Kodriano, E. Poem, R. Presman, D. Galushko, P. M. Petroff, and D. Gershoni, Coherent optical writing and reading of the exciton spin state in single quantum dots, *Physical Review Letters* **106**, 040504 (2011).
- [8] I. Favero, G. Cassabois, R. Ferreira, D. Darson, C. Voisin, J. Tignon, C. Delalande, G. Bastard, P. Roussignol, and J. M. Grard, Acoustic phonon sidebands in the emission line of single InAs/GaAs quantum dots, *Physical Review B - Condensed Matter and Materials Physics* **68**, 233301 (2003).
- [9] A. S. Bracker, M. Scheibner, M. F. Doty, E. A. Stinaff, I. V. Ponomarev, J. C. Kim, L. J. Whitman, T. L. Reinecke, and D. Gammon, Engineering electron and hole tunneling with asymmetric InAs quantum dot molecules, *Applied Physics Letters* **89**, 233110 (2006).
- [10] F. Martins, F. K. Malinowski, P. D. Nissen, E. Barnes, S. Fallahi, G. C. Gardner, M. J. Manfra, C. M. Marcus, and F. Kuemmeth, Noise suppression using symmetric exchange gates in spin qubits, *Physical Review Letters* **116**, 116801 (2016).
- [11] D. Kim, S. G. Carter, A. Greulich, A. S. Bracker, and D. Gammon, Ultrafast optical control of entanglement between two quantum-dot spins, *Nature Physics* **7**, 223 (2011).
- [12] H. J. Kimble, The quantum internet, *Nature* **453**, 1023 (2008).
- [13] S. E. Economou, N. Lindner, and T. Rudolph, Optically generated 2-dimensional photonic cluster state from coupled quantum dots, *Phys. Rev. Lett.* **105**, 093601 (2010).
- [14] R. Raussendorf and H. J. Briegel, A one-way quantum computer, *Physical Review Letters* **86**, 5188 (2001).
- [15] E. Zallo, R. Trotta, V. Kpek, Y. H. Huo, P. Atkinson, F. Ding, T. Sikola, A. Rastelli, and O. G. Schmidt, Strain-induced active tuning of the coherent tunneling in quantum dot molecules, *Physical Review B* **89**, 241303 (2014).
- [16] S. G. Carter, A. S. Bracker, M. K. Yakes, M. K. Zalalutdinov, M. Kim, C. S. Kim, B. Lee, and D. Gammon, Tunable coupling of a double quantum dot spin system to a mechanical resonator, *Nano Lett* **19**, 11 (2019).
- [17] G. Burkard, G. Seelig, and D. Loss, Spin interactions and switching in vertically tunnel-coupled quantum dots, *Phys. Rev. B* **62**, 2581 (2000).
- [18] M. Korkusiński and P. Hawrylak, Electronic structure of vertically stacked self-assembled quantum disks, *Phys. Rev. B* **63**, 195311 (2001).
- [19] D. Bellucci, F. Troiani, G. Goldoni, and E. Molinari, Neutral and charged electron-hole complexes in artificial molecules: Quantum transitions induced by the in-plane magnetic field, *Phys. Rev. B* **70**, 205332 (2004).
- [20] D. Jacob, B. Wunsch, and D. Pfannkuche, Charge localization and isospin blockade in vertical double quantum dots, *Phys. Rev. B* **70**, 081314 (2004).
- [21] L. G. D. D. Silva, J. M. Villas-Bas, and S. E. Ulloa, Tunneling and optical control in quantum ring molecules, *Physical Review B - Condensed Matter and Materials Physics* **76**, 155306 (2007).
- [22] J. I. Climente, Tuning the tunnel coupling of quantum dot molecules with longitudinal magnetic fields, *Applied Physics Letters* **93**, 223109 (2008).
- [23] J. Planelles, J. I. Climente, F. Rajadell, M. F. Doty, A. S. Bracker, and D. Gammon, *Phys. Rev. B* **82**, 155307 (2010).
- [24] J. Phoenix, M. Korkusinski, D. Dalacu, P. J. Poole, P. Zawadzki, S. Studenikin, R. L. Williams, A. S. Sachrajda, and L. Gaudreau, Magnetic tuning of tunnel coupling between InAsP double quantum dots in InP nanowires, *Scientific Reports* **12**, 5100 (2022).
- [25] H. J. Krenner, M. Sabathil, E. C. Clark, A. Kress, D. Schuh, M. Bichler, G. Abstreiter, and J. J. Finley, Direct observation of controlled coupling in an individual quantum dot molecule, *Physical Review Letters* **94**, 057402 (2005).
- [26] F. Bopp, J. Rojas, N. Revenga, H. Riedl, F. Sbresny, K. Boos, T. Simmet, A. Ahmadi, D. Gershoni, J. Kasprzak, A. Ludwig, S. Reitzenstein, A. Wieck, D. Reuter, K. Müller, and J. J. Finley, Quantum dot molecule devices with optical control of charge status and electronic control of coupling, *Advanced Quantum Technologies* **5**, 2200049 (2022).
- [27] P. W. Fry, J. J. Finley, L. R. Wilson, A. Lematre, D. J. Mowbray, M. S. Skolnick, M. Hopkinson, G. Hill, and J. C. Clark, Electric-field-dependent carrier capture and escape in self-assembled InAs/GaAs quantum dots, *Applied Physics Letters* **77**, 4344 (2000).
- [28] See supplemental material at [url will be inserted by publisher] for further details on the sample structure and theoretical models.
- [29] M. Bayer, S. Walck, and T. Reinecke, Exciton binding energies and diamagnetic shifts in semiconductor quantum wires and quantum dots, *Physical Review B - Condensed Matter and Materials Physics* **57**, 6584 (1998).
- [30] M. Bayer, O. Stern, A. Kuther, and A. Forchel, Spectroscopic study of dark excitons in $\text{In}_x\text{Ga}_{1-x}\text{As}$ self-assembled quantum dots by a magnetic-field-induced symmetry breaking, *Phys. Rev. B* **61**, 7273 (2000).
- [31] M. Bayer, G. Ortner, O. Stern, A. Kuther, A. A. Gorbunov, A. Forchel, P. Hawrylak, S. Fafard, K. Hinzer, T. L. Reinecke, S. N. Walck, J. P. Reithmaier, F. Klopff, and F. Schäfer, Fine structure of neutral and charged excitons in self-assembled $\text{In}(\text{Ga})\text{As}/(\text{Al})\text{GaAs}$ quantum dots, *Physical Review B - Condensed Matter and Materials Physics* **65**, 1953151 (2002).
- [32] L. Jacak, P. Hawrylak, and A. Wojs, *Quantum dots* (Springer Science & Business Media, 2013).
- [33] Z. Wasilewski, S. Fafard, and J. McCaffrey, Size and shape engineering of vertically stacked self-assembled quantum dots, *Journal of Crystal Growth* **201-202**, 1131 (1999).
- [34] R. Colombelli, V. Piazza, A. Badolato, M. Lazzarino, F. Beltram, W. Schoenfeld, and P. Petroff, Conduction-

band offset of single inas monolayers on gaas, Applied Physics Letters **76**, 1146 (2000).

Magnetic tuning of the tunnel coupling in an optical active quantum dot molecule Supplemental Material

Frederik Bopp,^{1,*} Charlotte Cullip,^{1,*} Christopher Thalacker,¹ Michelle Lienhart,¹ Johannes Schall,² Nikolai Bart,³ Friedrich Sbresny,⁴ Katarina Boos,⁴ Sven Rodt,² Dirk Reuter,⁵ Arne Ludwig,³ Andreas D. Wieck,³ Stephan Reitzenstein,² Filippo Troiani,⁶ Guido Goldoni,^{6,7} Elisa Molinari,^{6,7} Kai Müller,⁴ and Jonathan J. Finley^{1,†}

¹Walter Schottky Institut, School of Natural Sciences, and MCQST,
Technische Universität München, Am Coulombwall 4, 85748 Garching, Germany

²Institut für Festkörperphysik, Technische Universität Berlin, Hardenbergstraße 36, 10623 Berlin, Germany

³Lehrstuhl für Angewandte Festkörperphysik, Ruhr-Universität Bochum,
Universitätsstraße 150, 44801 Bochum, Germany

⁴Walter Schottky Institut, School of Computation, Information and Technology, and MCQST,
Technische Universität München, Am Coulombwall 4, 85748 Garching, Germany

⁵Paderborn University, Department of Physics, Warburger Straße 100, 33098 Paderborn, Germany

⁶Centro S3, CNR-Istituto Nanoscienze, Via Campi 213/a, 41125 Modena, Italy

⁷Dipartimento di Scienze Fisiche, Informatiche e Matematiche,
Università di Modena e Reggio Emilia, Via Campi 213/a, 41125 Modena, Italy

(Dated: March 23, 2023)

I. SAMPLE AND SETUP

The investigated QDM was grown by solid-source molecular beam epitaxy. It consisted of two vertically stacked InAs QDs, embedded in a GaAs matrix. The height of the top (bottom) QD was fixed to 2.9 nm (2.7 nm) via the In-flush technique during growth [1]. This height configuration facilitates electric field-induced tunnel coupling of orbital states in the conduction band. A wetting layer to wetting layer separation of 10 nm and an $\text{Al}_x\text{Ga}_{(x-1)}\text{As}$ barrier ($x = 0.33$) with a thickness of 2.5 nm placed between the dots determines the coupling strength at 0 T. A 50 nm thick $\text{Al}_x\text{Ga}_{(x-1)}\text{As}$ tunnel barrier ($x = 0.33$) was grown 5 nm below the QDM to prolong electron tunneling times. The molecule was embedded into a p-i-n diode, with the doped regions used as contacts to gate the sample. The diode contacts are placed more than 150 nm from the molecule to prevent uncontrolled charge tunneling into the QDM. Furthermore, a distributed Bragg reflector was grown below the diode and a circular Bragg grating is positioned deterministically via in-situ electron beam lithography above an individual QDM to improve photon in-

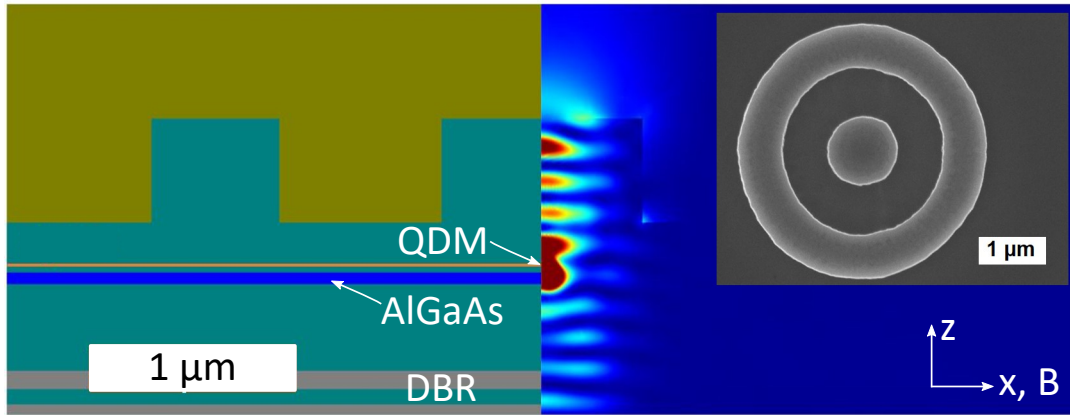


Fig. S1. Schematic of the sample design (left) and the simulated electric field distribution (right). A QDM is located at the interface of the two illustrations. The inset shows a scanning electron microscope image of the QDM-circular Bragg grating device.

* These authors contributed equally to this work

† finley@wsi.tum.de

and outcoupling efficiencies [2]. Figure S1 shows a schematic of the sample design (left) and simulated electric field distribution (right) calculated using JCMSuite [3]. The inset depicts a scanning electron microscope image of the circular Bragg grating. All measurements are performed at 10 K inside an Oxford Instruments magnet. A tunable diode laser is used to excite the QDM.

II. TWO-STATE MODEL

The neutral exciton in our system can be described by the following Hamiltonian:

$$H_X^0 = E_0 \cdot \hat{I} + \begin{bmatrix} \Gamma - edF & t \\ t & 0 \end{bmatrix} + \hat{H}_{QCSE}, \quad (1)$$

where E_0 is the zero-field energy of the direct exciton, \hat{I} is the identity matrix, Γ is the energy needed to move an electron from the upper to the lower dot, and t is the tunnel coupling. edF accounts for the Stark shift for inter-dot excitons, with e the electron charge, d the separation between electron and hole, and F the electric field. The final term \hat{H}_{QCSE} accounts for the energy shift from the quantum-confined Stark-effect, and is given by

$$\Delta E_{QCSE} = \vec{p} \cdot \vec{F} + \beta F^2, \quad (2)$$

where \vec{p} is the dipole moment and β is the polarizability. Solving the full Hamiltonian gives the following eigenvalues:

$$E_{\pm} = \frac{1}{2}(2E_0 - edF + \Gamma + 2\Delta E_{QCSE}) \quad (3)$$

$$\pm \sqrt{(edF - \Gamma)^2 + (2t)^2}. \quad (4)$$

In the main manuscript, these energies for the symmetric (dotted pink) and anti-symmetric (dotted green) eigenstates are shown in Figure 1 (b). The splitting ΔE between these eigenenergies is then given as

$$\Delta E = \sqrt{(edF - \Gamma)^2 + (2t)^2}, \quad (5)$$

where $2t$ is the minimum splitting between the two eigenstates, i.e. at the avoided crossing. This equation is used for fitting the data points in Figure 3 (a) of the main manuscript.

III. SINGLE PARTICLE STATES IN 3D CONFINEMENT POTENTIAL

To solve Equation 2 of the main manuscript, we discretize the confinement potential on a real-space grid of $N = N_1 \times N_2 \times N_3$ points, where $N = 64 \times 64 \times 128$. The simulation space has a size of $700 \times 700 \times 220 \text{ nm}^3$. Each point is identified by the vector $\mathbf{r}_i = \sum_{k=1}^3 (\lambda_i^k - N_k/2) \Delta_k \mathbf{e}_k$, with $\lambda_i^k = 1, \dots, N_k$ and $\mathbf{e}_{1,2,3} = \mathbf{x}, \mathbf{y}, \mathbf{z}$. By rephrasing the resulting finite-difference equation, we obtain a discrete eigenvalue problem:

$$\sum_{j=1}^N \left\{ \frac{1}{2m_{\chi}^*} \left[-\hbar^2 (\nabla^2)_{ij} + \frac{2i\hbar q_{\chi}}{c} (\mathbf{A} \cdot \nabla)_{ij} + \frac{q_{\chi}^2}{c^2} (\mathbf{A}^2)_{ij} \right] + V_{ij}^{\chi} \right\} \phi_{\alpha,j}^{\chi} = \epsilon_{\alpha} \phi_{\alpha,i}^{\chi}, \quad (6)$$

where $\phi_{\alpha,i}^{\chi} = \phi_{\alpha}^{\chi}(\mathbf{r}_i)$ is the eigenstate of the Hamiltonian, $\chi = e, h$ for electrons and holes, and $q_h = -q_e = |e|$. In the real-space basis, the vector- and confining-potential operators are diagonal, thus $V_{ij}^{\chi} = \delta_{i,j} V_{\chi}(\mathbf{r}_i)$ and $(\mathbf{A}^2)_{ij} = \delta_{i,j} [\mathbf{A}(\mathbf{r}_i)]^2$. When applying the differential operator on the wave function $\phi_{\alpha,i}^{\chi}$, we obtain:

$$\sum_{j=1}^N (\nabla^2)_{ij} \phi_{\alpha,j} = \sum_{k=1}^3 \frac{\phi_{\alpha}(\mathbf{r}_i + \Delta_k \mathbf{e}_k) - 2\phi_{\alpha}(\mathbf{r}_i) + \phi_{\alpha}(\mathbf{r}_i - \Delta_k \mathbf{e}_k)}{\Delta_k^2} \quad (7)$$

and

$$\sum_{j=1}^N (\mathbf{A} \cdot \nabla)_{ij} \phi_{\alpha,j} = \sum_{k=1}^3 A_{k,i} \frac{\phi_{\alpha}(\mathbf{r}_i + \Delta_k \mathbf{e}_k) - \phi_{\alpha}(\mathbf{r}_i - \Delta_k \mathbf{e}_k)}{2\Delta_k}, \quad (8)$$

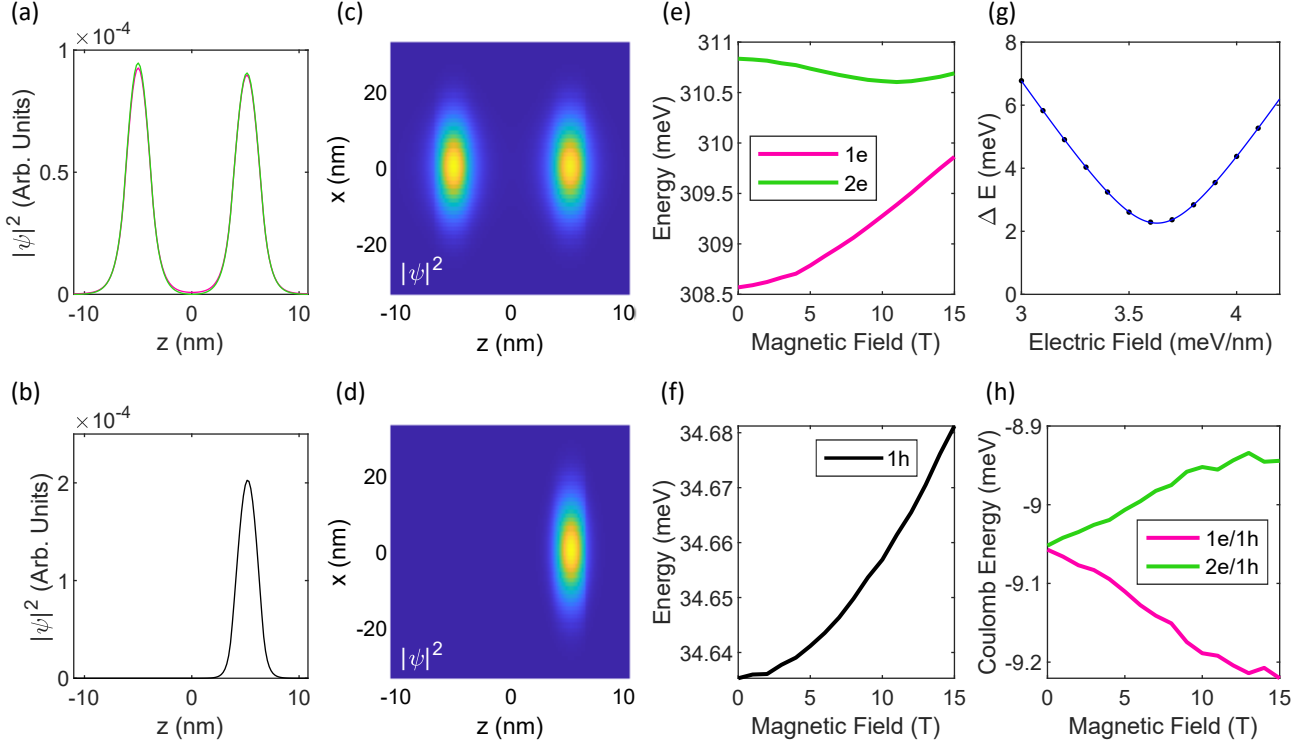


Fig. S2. (a): Absolute value of the wave function along the growth axes of the lowest (pink) and second lowest (green) electron eigenstate at resonance, and of the lowest hole eigenstate (b). (c) and (d): Two dimensional wave function along \mathbf{x} and \mathbf{z} for the lowest electron and hole eigenstate, respectively. (e) and (f) magnetic field dependent energy of the two lowest electron and lowest hole eigenstate, respectively. (g): Energy difference of the two lowest electron eigenstates for varying bias (black). The data points are fitted using equation 5 (blue) (h) Coulomb energy between the lowest (second lowest) electron and lowest hole eigenstate in pink (green).

where $A_{k,i} = A_k(\mathbf{r}_i)$.

The Hamiltonian is calculated for a 3D-potential, which consists of an asymmetric double square well along the \mathbf{z} direction and parabolic potentials along the \mathbf{x} and \mathbf{y} direction. The square wells have a width of $d_1 = 2.7$ nm and $d_2 = 2.9$ nm, which corresponds to the height of the bottom and top QD, respectively. The potential depth $V_0 = 690$ meV matches the conduction band offset between GaAs and InAs. An electric field equivalent to 3.63 meV/nm is included into the model to facilitate the hybridisation of the two lowest electron eigenstates. The model is calibrated by setting the effective electron mass m_e^* , as the only free parameter, such that the energy gap between the two lowest eigenstates matches the experimental results. We obtain an effective mass of $m^* = 0.0495 m_{e,0}$ ($m_{e,0}$ is the free-electron mass), which is between the recommended effective masses of GaAs ($m_{\text{GaAs}}^* = 0.067$) and InAs ($m_{\text{InAs}}^* = 0.023$) [4]. A magnetic field is applied along the in-plane direction \mathbf{x} .

Figure S2 (a) and (b) show the absolute value of the electron and hole wave functions along the growth direction \mathbf{z} at 0 T. The green (pink) data set represents the lowest (second lowest) electron eigenstate ϕ_1^e (ϕ_2^e). Hereafter we refer to them as e1 and e2, respectively. Panels (c) and (d) show surface plots of the wave function for the lowest electron and hole eigenstate, respectively. The magnetic field dependent single particle energies of e1, e2 and the lowest hole eigenstate are shown in panels (e) and (f), respectively. Bias sweeps are performed to ensure that the simulations are performed at the coupling condition. Figure S2 (g) shows the energy difference between e1 and e2 as a function of the bias at 0 T. The energy difference is fitted by equation 5 to obtain the resonance bias and the minimum energy splitting.

In the experiment, we analyze the energy splitting ΔE of the neutral exciton, instead of a single particle state. To account for the Coulomb interaction, we calculate the direct matrix involving e1, e2 and the lowest energy hole state h1. The direct and attractive Coulomb matrix elements are given by:

$$V_{\alpha\beta}^{eh} = \iint \frac{[\phi_{\alpha}^e(\mathbf{r})]^* [\phi_{\beta}^h(\mathbf{r}')]^* \phi_{\beta}^h(\mathbf{r}') \phi_{\alpha}^e(\mathbf{r})}{\kappa_r |\mathbf{r} - \mathbf{r}'|} d\mathbf{r} d\mathbf{r}', \quad (9)$$

where κ_r is the static dielectric constant of the semiconductor medium. The matrix elements are numerically calculated

from the expression

$$V_{\alpha\beta\gamma\delta}^{\chi\chi'} = \pm \frac{e^2}{\kappa} \int \mathcal{F}^{-1} \left[\frac{1}{k^2} \tilde{\Phi}_{\alpha\beta}^{\chi}(\mathbf{k}) \right] \Phi_{\gamma\delta}^{\chi'}(\mathbf{r}) d\mathbf{r}, \quad (10)$$

where $\Phi_{\alpha\beta}^{\chi}(\mathbf{r}) = [\phi_{\alpha}^{\chi}(\mathbf{r})]^* \phi_{\beta}^{\chi}(\mathbf{r})$, and $\tilde{\Phi}_{\alpha\beta}^{\chi}(\mathbf{k}) = \mathcal{F}[\phi_{\alpha\beta}^{\chi}(\mathbf{r})]$ is its Fourier transform.

The exciton energy is then computed by including the Coulomb interaction in first-order perturbation theory:

$$E_{X_{0,l}} = \epsilon_l^e + \epsilon_1^h + V_{l11}^{eh}, \quad (11)$$

where $l = 1, 2$ specifies the involved electron state and the corresponding exciton. The energy splitting ΔE plotted in Figure 2 (b) incorporates the single particle energy difference ΔE_{SP} as well as the difference in Coulomb energy ΔE_C , and is given by:

$$\Delta E^{Th} = E_{X_{0,2}} - E_{X_{0,1}} = \epsilon_2^e - \epsilon_1^e + V_{2211}^{eh} - V_{1111}^{eh} = \Delta E_{SP} + \Delta E_C. \quad (12)$$

Figure S2 (h) shows the Coulomb energy between e1 (e2) and lowest energy hole state in pink (green).

-
- [1] Z. Wasilewski, S. Fafard, and J. McCaffrey, Size and shape engineering of vertically stacked self-assembled quantum dots, *Journal of Crystal Growth* **201-202**, 1131 (1999).
 - [2] J. Schall, M. Deconinck, N. Bart, M. Florian, M. Helvesen, C. Dangel, R. Schmidt, L. Bremer, F. Bopp, I. Hüllen, C. Gies, D. Reuter, A. D. Wieck, S. Rodt, J. J. Finley, F. Jahnke, A. Ludwig, and S. Reitzenstein, Bright electrically controllable quantum-dot-molecule devices fabricated by in situ electron-beam lithography, *Advanced Quantum Technologies* **4**, 2100002 (2021).
 - [3] J. Pomplun, S. Burger, L. Zschiedrich, and F. Schmidt, Adaptive finite element method for simulation of optical nano structures, *physica status solidi (b)* **244**, 3419 (2007).
 - [4] N. Bouarissa and H. Aourag, Effective masses of electrons and heavy holes in InAs, InSb, GaSb, GaAs and some of their ternary compounds, *Infrared Physics & Technology* **40**, 343 (1999).